Bull. Chem. Soc. Ethiop. **2025**, 39(10), 2005-2026.
DOI: https://dx.doi.org/10.4314/bcse.v39i10.10

ISSN 1011-3924
Printed in Ethiopia
Online ISSN 1726-801X

STRUCTURAL, DOCKING, MOLECULAR DYNAMICS AND ANTIBACTERIAL ANALYSIS OF THYMOPENTIN: A POTENT ANTI-CANCER, -COVID-19 AND VIRAL

Alev Er[1], Sefa Celik[1*], Elif Cakir[2], Aysen E. Ozel[1], Sevim Akyuz[3]

[1]Physics Department, Science Faculty, Istanbul University, Vezneciler, 34134, Istanbul, Turkey
[2]Department of Food Engineering, Engineering Faculty, Istanbul Aydin University, PO Box 38, 34295, Kucukcekmece, Istanbul, Turkey
[3]Physics Department, Science and Letters Faculty, Istanbul Kultur University, Atakoy Campus, Bakirkoy 34156, Istanbul, Turkey

(Received March 12, 2025; Revised April 26, 2025; Accepted June 2, 2025)

ABSTRACT. To gain deeper insights into the biological activity of thymopentin, its structural, anticancer, antiviral and antimicrobial properties were systematically investigated. Conformational preferences of thymopentin were investigated through conformational analysis and the lowest energy conformation was optimized using density functional theory (DFT) method, Becke three Lee–Yang–Parr (B3LYP) functional and 6-31G(d,p) basis set. Vibrational wavenumbers of the optimized structure were computed and compared with the experimental results. To elucidate the potential of thymopentin as anti-COVID-19 and anticancer agents, molecular docking simulations were performed. Thymopentin was docked into DNA (PDB ID: 1BNA), SARS-CoV-2 main protease (PDB ID: 6M03) and EGFR receptor complex (PDB ID: 4HJO). Additionally, following molecular docking analyses, top-scoring ligand-receptor complexes of thymopentin with SARS-CoV-2 enzyme (6M03) and EGFR (4HJO) were subjected to 50 ns all-atom molecular dynamics (MD) simulations to examine the ligand-receptor interactions in greater detail. Moreover, the antimicrobial potency of thymopentin against the most prevailing human pathogenic microorganisms was also investigated. The strongest antibacterial activity was observed against "*Listeria monocytogenes*", a pathogenic bacterium capable of causing listeriosis, a serious infection that can potentially lead to death. This study revealed the anticancer, anti-Covid 19 and antimicrobial activities of the thymopentin molecule, demonstrating its multifunctional bioactivity.

KEY WORDS: Thymopentin, DFT calculations, Vibrational analysis, Molecular docking, Molecular dynamics

INTRODUCTION

Thymopentin (TP-5), a pentapeptide (Arg-Lys-Asp-Val-Tyr), contains of amino acid residues 32-36 of the thymic hormone thymopoietin which compose of 49 amino acid residues. Due to its whole range of biological functions, it can be thought of as the active site of thymic hormone thymopoietin, a polypeptide hormone released by the thymus's epithelial cells [1]. The thymus gland, located in the mediastinum behind the sternum, is a vital organ for the growth of the immune system of body, comprises two similar lobes, each split into a peripheral cortex and a central medulla [2]. The importance of thymopentin, TP5, or thymopoietin pentapeptide in dermatology has been demonstrated due to its immunological effects and immunoreactive qualities in treating patients with alopecia areata, atopic dermatitis, Sézary syndrome, and scleroderma [3]. Gallo *et al.* (1993) reported that a series of immune abnormalities that were detected before the development and growth of carcinogen-induced rat mammary tumors were significantly restored by the thymic pentapeptide thymopentin and tumor appearance and growth were delayed [4]. It was shown that The TP5 alleviates immunosuppression in tumor-bearing mice and has mild immunoregulatory effects on a host [4]. For a long time, TP5 was thought to be a possible treatment for immune disorders and cancer. Investigation into cancer

*Corresponding author. E-mail: scelik@istanbul.edu.tr

therapy continues to focus on the uptake of anticancer agents in solid tumors. Drug resistance and minimal efficacy are the results of many anticancer medications, like doxorubicin, which only migrate 40–50 μm (3-5 cells in diameter) from the vasculature [5].

To fully capitalize on the peptide's powerful effects on tumor cells, more effective methods of delivering TP5 to target tumor cells must be developed, as the pleiotropy and limited activity of TP5 in cancer therapy may be caused by poor TP5 penetration into tumor cells [6]. In numerous animal model systems and human in vitro experiments, the 49 naturally occurring amino acids found in thymic hormones have demonstrated immunoregulatory activity. The synthetic pentapeptide TP5 matches this hormone's active structure [7]. The combination of chemotherapy and immunotherapy appears to be a more effective anti-cancer treatment than chemotherapy alone. Additionally, including immunotherapy can greatly lower the severe hematological toxicity associated with most chemotherapeutic clinical investigations [8]. To cure cancer, TP5 has lately been investigated as an immunotherapeutic drug [9].

Thymopentin at a high dose can greatly increase the antiviral effectiveness of adefovir dipivoxil when taken together. Additionally, it fulfills the special needs of these patients and makes it easier to provide medication to those who have severe hepatitis B [10].

One of the treatment drugs employed throughout the COVID-19 pandemic in China was thymopentin (Arg-Lys-Asp-Val-Tyr, RKDVY, TP5), an immunomodulatory pentapeptide that is the active core of the thymus hormone, thymopoietin [11].

Thymopentin, a pentapeptide generic metabolite, has immune-boosting properties and is the active site of the naturally occurring hormone thymopoietin. It promotes the growth of thymic T cells and may aid immunocompromised individuals in regaining their immunocompetence [1]. Thymopentin is modified with myristic acid for enhanced immunomodulation and plasma stability [12]. By boosting the immune system, thymopentin could potentially be an effective substitute for managing this new coronavirus [13].

There hasn’t been any prior research on the thymopentin molecule’s molecular structure and vibrational spectroscopy. The most stable conformation was identified through conformational analysis, and the most stable conformer was then optimized using density functional theory (DFT) with hybrid functional (B3LYP), a very effective technique in the study of molecules’ electronic structures nowadays, using the DFT/B3LYP/6-31G(d,p) level of theory [14].

In this study, the most stable conformation was identified through conformational analysis, geometry optimization was carried out, charge transfer interaction was obtained through HOMO-LUMO and MEP calculations, and FTIR and Raman analysis were conducted to uncover the structural information of the thymopentin molecule. The technique of molecular docking was then used to examine thymopentin’s anti-cancer and anti-COVID-19 activity, highlighting its significance for drug development and its interactions with DNA (PDB IDs: 1BNA), SARS-CoV-2 main protease (PDB ID: 6M03), and EGFR (PDB ID: 4HJO) receptor complex. Then, using the molecular docking method, the anticancer and anti-COVID-19 activity of thymopentin was examined to emphasize its crucial role in drug development and its interactions with DNA, SARS-CoV-2 main protease, and EGFR receptor complex (PDB IDs: 1BNA, 6M03, and 4HJO, respectively). The ligand-receptor complexes of thymopentin with the EGFR receptor complex (4HJO) and SARS-CoV-2 enzyme (6M03) were then simulated using molecular dynamics (MD).

EXPERIMENTAL

Thymopentin (CAS Number 69558-55-0) was purchased in solid form from Sigma-Aldrich and used precisely as directed. A Jasco 6300 FT-IR spectrometer with a resolution of 2 cm^{-1} was used to record the FTIR spectra of the Thymopentin KBr disk. The sample’s Raman spectra were recorded using a Jasco NRS 3100 micro-Raman spectrometer, which has a 532 nm diode

laser and a 1200 lines/mm diffraction grating. The 520 cm^{-1} silicon phonon mode was employed for calibration.

Antimicrobial activity and antibacterial activity

For antimicrobial activity, its effect on *Staphylococcus aureus*, *Listeria monocytogenes*, *Bacillus cereus* from gram-positive bacteria and *Salmonella typhimurium* and *Escherichiae coli* from Gram-negative bacteria were determined. All pathogenic bacteria were activated on nutrient agar at 37 °C, single colonies were enriched in broth and used. Pathogens activated at 37 ^{o}C were inoculated into 1% nutrient agar. Thymopentin was diluted (1:1, w/v) in sterile distilled water. 100 µL of the sample was transferred to the opened wells and inhibition zones were measured after 24 hours at 37 ^{o}C. Sterile water was used as negative control. Diameter measurements are evaluated in mm [15, 16].

Antifungal activity

Potato dextrose agar was smeared with *Aspergillus niger*, *Penicillium expansum* cultures for 24 hours for antifungal activity. 100 µL of sample was transferred to the opened wells and incubated at 30 ^{o}C for 24 hours. Inhibition diameter measured in mm [17].

Computational details

The thymopentin molecule was conformationally investigated via the Spartan06 program [18] by the PM3 method. Then, using the Gaussian 16 software package [19] and the DFT/B3LYP/6-31G(d,p) level of theory, the derived minimum energy conformer was optimized. Since the thymopentin molecule contains a large number of atoms and has a flexible structure, calculations could not be made with high basis sets, but, the 6-31G(d,p) basis set has been shown to be a good choice as it's optimized geometries were close to the geometries obtained by larger basis sets [20]. Using MOLVIB software [21] and the scaled quantum mechanical force field approach described by Pulay *et al.* [22], the harmonic force field of thymopentin was investigated. The Cartesian coordinate force fields were transformed into natural internal coordinates, and the IR intensity, Raman activity, and potential energy distribution (PED) of vibration modes were determined. Using the simulation application Simirra [23], the computed Raman activities were converted to theoretical Raman intensities. Lorentzian band forms with a bandwidth (FWHM) of 10 cm^{-1} were utilized for the theoretical spectral simulations.

The wavenumbers calculated using the DFT/B3LYP/6-31G(d,p) level of theory were scaled by scaling factors (O-H stretch 0.87; N-H stretch 0.84; C-H stretch 0.91; C-O and C=O stretch 0.86; O-H, N-H and C-H deformation 0.92; O-H, NH stretch (involving H-bonds) 0.98; all others 0.98) taken from earlier research [24, 25] to ensure a reasonable agreement between experimental and calculated wavenumbers and then optimized by fitting the measured frequencies to the computed.

RESULTS AND DISCUSSION

Antimicrobial and antifungal activity

In the study, the in vitro antimicrobial activity of the compound on the agar plate was determined on gram positive and gram negative bacteria and the results are presented in table 1. Antibacterial activity was observed in gram-positive bacteria *L. monocytogenes* and *B. cereus.* The highest antibacterial effect (12 mm) was determined against L. monocytogenes. İt is dangerous bacteria that can cause serious effects on the nervous system that may result in death

by causing Listeriosis in the elderly, children, pregnant women and patients with suppressed immune systems [26].

It did not show any effect on *S. aureus* from gram-positive bacteria and against gram-negative bacteria. Thymopentin compound has been determined to have an antimicrobial effect against gram-positive bacteria. Penicillium is considered an asthma agent in children and adults [27]. Antifungal activity was seen against *P.expansum*.

Table 1. Antimicrobial activity of thymopentin.

Antimicrobial	Zone (mm)
Antibacterial	
Gram (+) bacteria	
Listeria monocytogenes	12.0±0.05
Bacillus cereus	0.9±0.1
Staphylococcus aureus	-
Gram (-) bacteria	-
Salmonella typhimurium	-
Esherichiae coli	-
Antifungal	
Aspergillus niger	-
Penicillium expansum	0.9±0.1

Structure

The most stable molecule structure was found by optimizing the lowest energy conformer, which was the outcome of the conformation analysis, utilizing the DFT/B3LYP/6-31G(d,p) level of theory. Figure 1 displays the optimized molecular structure of the thymopentin molecule.

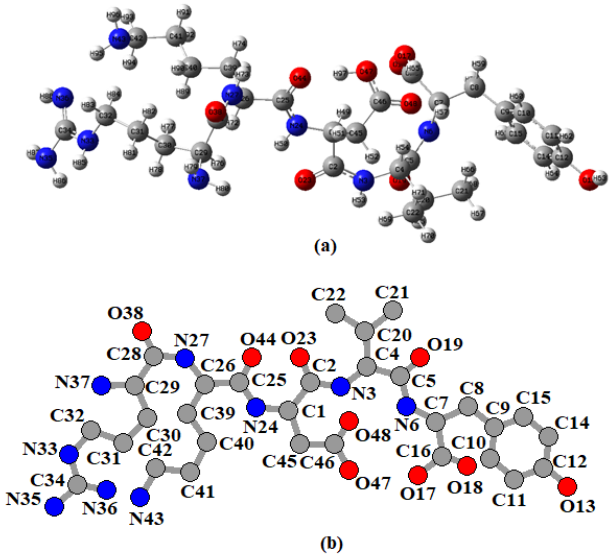

Figure 1. The optimized molecular structure of the thymopentin molecule (a), the 2D schema of thymopentin (For clarity H atoms were not shown) (b).

This study is the first to do the conformational analysis and geometry optimization of the thymopentin molecule; no experimental studies have been published in the literature before this work. For this reason, we compared calculated values of a synthetic pentapeptide thymopentin (Arg-Lys-Asp-Val-Tyr) with those of corresponding monopeptides.

The bond lengths between the atoms N35-C34, N36-C34, N33-C34, N33-C32, C32-C31, C31-C30, C30-C29, C29-N37 and C29-C28 of arginine moiety of thymopentin were computed as 1.403, 1.290, 1.381, 1.462, 1.532, 1.538, 1.547, 1.463, and 1.547 Å, respectively, and the corresponding bond lengths of arginine crystal [28] were 1.319, 1.320, 1.323, 1.473, 1.520, 1.520, 1.520, 1.470, and 1.520 Å, respectively.

The bond lengths between the atoms N27-C26, C26-C25, C39-C26, C40-C39, C41-C40 and C42-C41 of lysine moiety of thymopentin were computed as 1.456, 1.535, 1.549, 1.530, 1.531 and 1.539 Å, respectively. The corresponding experimental bond lengths of lysine monopeptide were reported as 1.495, 1.529, 1.524, 1.526, 1.516, and 1.511 Å, respectively [29].

The bond lengths between the atoms N24-C1, C2-C1, C45-C1 and C46-C45 of the aspartic acid moiety of thymopentin were computed as 1.458, 1.559, 1.566, and 1.525 Å, respectively, and the corresponding experimental values for aspartic acid were 1.495, 1.543, 1.518, and 1.512 Å, respectively [30].

The bond lengths between the atoms N3-C4, C4-C5, C4-C20, C20-C21 and C20-C22 of valine moiety of thymopentin were computed as 1.467, 1.548, 1.560, 1.535 and 1.534 Å, respectively, and the corresponding experimental values of crystalline valine were 1.495, 1.518, 1.546, 1.568 and 1.534 Å, respectively [31].

The bond lengths between the atoms C7-N6, C7-C16, C8-C7, C8-C9, C9-C10, C10-C11,C11-C12, C9-C15, C15-C14, C14-C12 and C12-O13 of tyrosine moiety of thymopentin were computed as 1.456, 1.543, 1.555, 1.511, 1.400, 1.394, 1.399, 1.403, 1.392, 1.399 and 1.366 Å, respectively, and for crystalline tyrosine the corresponding values were found to be 1.485, 1.533, 1.542, 1.510, 1.410, 1.391, 1.397, 1.401, 1.392, 1.395 and 1.372 Å, respectively. [32].
The results indicated that all the geometrical parameters of the studied compound are found to be in conformity with the structural data of similar compounds.

Vibrational spectral analysis

With 97 atoms, the thymopentin molecule ($C_{30}H_{49}N_9O_9$) has 285 normal modes of vibration. Utilizing the DFT/B3LYP/6-31G(d,p) level of theory, the vibrational frequencies of the thymopentin molecule were computed and compared to the experimental data to determine its spectroscopic signature. And also it is important to note that the experimental spectrum for thymopentin was recorded in the solid phase, whereas the computed spectrum was in the gas phase. The theoretical and experimental IR spectra of thymopentin are displayed in figure 2 and its theoretical and experimental Raman spectra are displayed in figure 3.

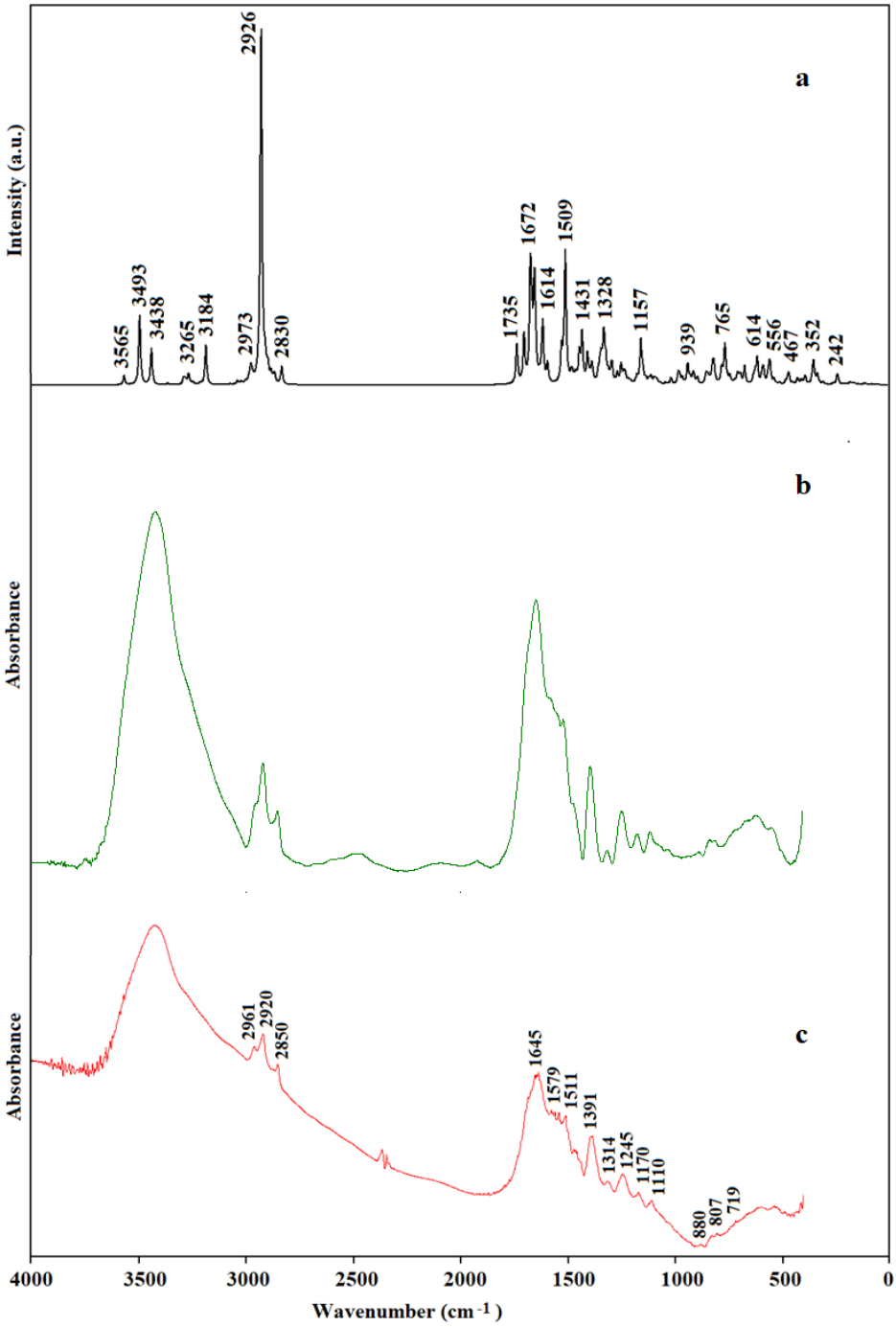

Figure 2. The theoretical IR (a), and baseline corrected experimental (b) and original experimental (c) FTIR spectra of thymopentin.

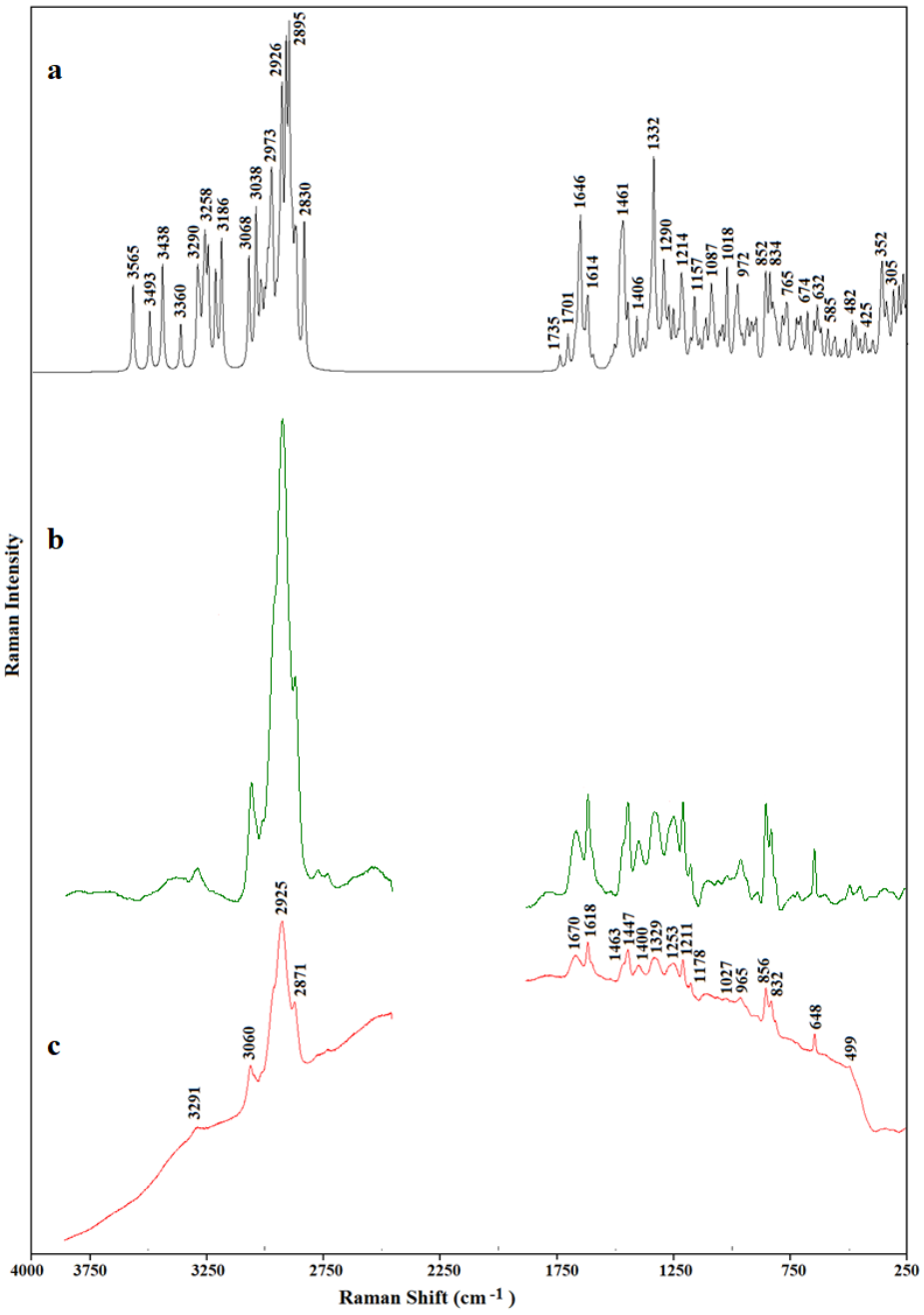

Figure 3. The theoretical (a), baseline corrected experimental (b) and original experimental (c) Raman spectra of thymopentin.

The theoretical harmonic vibrational wavenumbers at the DFT/B3LYP/6-31G(d,p) level of theory, the calculated IR and Raman intensities, the PED, and the experimental vibrational wavenumbers obtained from the IR and Raman spectra of solid thymopentin are displayed in table 2. The present investigation examined peptide group vibrations, namely C=O, C–N stretching, and N–H in-plane bending, in addition to C–H stretching, O–H bending, O–H stretching, N–H stretching, and other modes.

The calculated O-H stretching modes were found at 3565, 3493, and 2926 cm^{-1} wavenumbers and were observed in 2920 (IR) and 2925 cm^{-1} (Raman). Except for O47–H97, the computed bond distances for the O–H groups are in the range of 0.966 and 0.983 Å. Intramolecular hydrogen bonding caused the O47–H97 (1.012 Å) bond to elongate by around 0.04 Å; as a result, the stretching wavenumber of this O–H bond dropped to 2926 cm^{-1}.

The N–H stretching mode of solid thymopentin was identified as the band at 3291 cm^{-1} detected in the experimental Raman spectra. The thymopentin's N–H stretching modes were predicted to be in the intervals of 3438–3184 cm^{-1}.

The C–H stretching modes of the Thymopentin according to examination were computed within the range of 3068–2830 cm^{-1}. The CH stretching vibrations of glycine, alanine, and serine amino acids were found in the intervals 2985–2873 cm^{-1} (IR), 3013–2870 cm^{-1} (Ra), and 2964–2853 cm^{-1} (IR), respectively [33-34].

Table 2. The calculated DFT/B3LYP/6-31G(d,p) and experimental wavenumbers (cm^{-1}) of thymopentin and the PED distributions of the vibration modes.

	Experimental		Calculated B3LYP			
Assignment	FTIR	Raman	ν^{S}	I(IR)	I (Raman)	PED %
ν_{OH} (Tyr)			3565	54	25	ν_{OH} (100)
ν_{OH} (Tyr)			3493	403	17	ν_{OH} (97)
ν_{NH} (Lys-NH_2)			3438	211	31	ν_{NH} (100)
ν_{NH} (Arg-NH_2)			3360	12	14	ν_{NH} (99)
ν_{NH} (Arg-NH)			3290	10	28	ν_{NH} (100)
ν_{NH} (Tyr)		3291	3286	32	30	ν_{NH} (100)
ν_{NH} (Lys-NH)			3279	29	24	ν_{NH} (100)
ν_{NH} (Val)			3265	60	27	ν_{NH} (99)
ν_{NH} (Arg-NH_2)			3258	10	40	ν_{NH} (100)
ν_{NH} (Arg-NH_2)			3253	3	35	ν_{NH} (100)
ν_{NH} (Lys-NH_2)			3243	16	36	ν_{NH} (100)
ν_{NH} (Arg-NH)			3210	10	29	ν_{NH} (100)
ν_{NH} (Arg-NH_2)			3186	4	37	ν_{NH} (100)
ν_{NH} (Asp)			3184	226	38	ν_{NH} (98)
ν_{CH} (Tyr-CH)		3060	3068	5	33	ν_{CH} (100)
ν_{CH} (Tyr-CH)			3038	5	47	ν_{CH} (94)
ν_{CH} (Asp-CH_2)			3038	1	47	ν_{CH} (99)
ν_{CH} (Tyr-CH)			3036	17	45	ν_{CH} (98)
ν_{CH} (Tyr-CH)			3018	17	26	ν_{CH} (99)
ν_{CH} (Val-CH)			3012	0	25	ν_{CH} (98)
ν_{CH} (Val-CH_3)			3000	10	24	ν_{CH} (99)
ν_{CH} (Tyr-CH)			2993	4	26	ν_{CH} (97)
ν_{CH} (Arg-CH_2)			2988	3	35	ν_{CH} (91)
ν_{CH} (Val-CH_3)			2982	27	38	ν_{CH} (99)
ν_{CH} (Lys-CH_2)			2976	19	49	ν_{CH} (89)
ν_{CH} (Arg-CH_2)			2974	27	55	ν_{CH} (88)
ν_{CH} (Val-CH_3)			2973	38	57	ν_{CH} (88)
ν_{CH} (Asp-CH_2)			2970	7	58	ν_{CH} (100)
ν_{CH} (Lys-CH)			2968	20	53	ν_{CH} (87)

ν_{CH} (Val-CH_3)	2961		2964	14	38	ν_{CH} (91)
ν_{CH} (Tyr-CH_2)			2951	7	26	ν_{CH} (98)
ν_{CH} (Arg-CH_2)			2941	14	37	ν_{CH} (97)
ν_{CH} (Lys-CH_2)			2935	12	52	ν_{CH} (90)
ν_{CH} (Arg-CH_2)			2931	24	69	ν_{CH} (91)
$\boldsymbol{\nu_{OH}}$ (Asp)	2920	2925	2926	1974	82	ν_{OH} (98)
ν_{CH} (Lys-CH_2)			2924	52	72	ν_{CH} (95)
ν_{CH} (Val-CH_3)			2911	9	88	ν_{CH} (94)
ν_{CH} (Tyr-CH_2)			2909	17	96	ν_{CH} (99)
ν_{CH} (Lys-CH_2)			2908	16	95	ν_{CH} (95)
ν_{CH} (Arg-CH)			2907	64	92	ν_{CH} (91)
ν_{CH} (Val-CH_3)			2901	26	71	ν_{CH} (93)
ν_{CH} (Arg-CH_2)			2895	28	100	ν_{CH} (93)
ν_{CH} (Lys-CH_2)			2895	44	100	ν_{CH} (93)
ν_{CH} (Val-CH)			2894	5	98	ν_{CH} (95)
ν_{CH} (Asp-CH)			2884	4	50	ν_{CH} (99)
ν_{CH} (Lys-CH_2)			2880	49	44	ν_{CH} (95)
ν_{CH} (Lys-CH_2)		2871	2871	12	42	ν_{CH} (93)
ν_{CH} (Arg-CH_2)	2850		2864	52	41	ν_{CH} (95)
ν_{CH} (Lys-CH_2)			2830	103	43	ν_{CH} (94)
ν_{CO} (Tyr-COOH)			1735	230	5	ν_{CO} (79)
ν_{CN}			1701	272	11	ν_{CN} (84)
ν_{CO} (Asp-COOH)		1670	1672	622	10	ν_{CO} (67) + δ_{COH} (9)
ν_{CO} (Val-amide I)			1665	199	13	ν_{CO} (66) + ν_{CN} (12)
ν_{CO} (Asp-amide I)			1655	252	33	ν_{CO} (53) + ν_{CN} (14)
ν_{CO} (Arg-amide I)	1645		1651	405	36	ν_{CO} (64) + ν_{NC} (8) + δ_{NCC} (6)
ν_{CC}			1646	50	45	ν_{CC} (61)
δ_{HNH}			1630	27	13	δ_{HNH} (39) + δ_{CNH} (31) + Γ_{CCNH} (16)
ν_{CC}			1620	16	20	ν_{CC} (68) + δ_{COH} (5)
δ_{HNH}		1618	1620	40	20	δ_{HNH} (45) + δ_{CNH} (37)
ν_{CO} (Lys-amide I)			1614	326	22	ν_{CO} (58) + ν_{CN} (24)
δ_{HNH}	1579		1592	110	5	δ_{HNH} (48) + δ_{CNH} (30) + ν_{CN} (11)
ν_{CN}			1527	179	3	ν_{CN} (44) + δ_{CNH} (39)
ν_{CC}			1516	76	5	ν_{CC} (35) + ν_{CO} (9) + δ_{CCH} (7)
ν_{CN}	1511		1509	729	5	ν_{CN} (33) + δ_{CNH} (29) + ν_{CC} (9) + ν_{CO} (6)
δ_{HCH}			1501	18	8	δ_{HCH} (27) + Γ_{HCCH} (13) + δ_{NCH} (8) + Γ_{CCCH} (6)
Γ_{HCCH}			1491	3	8	Γ_{HCCH} (28) + δ_{HCH} (16)
δ_{HCH}			1482	20	24	δ_{HCH} (58)
δ_{HCH}			1480	23	30	δ_{HCH} (19) + Γ_{CCCH} (13) + Γ_{HCCH} (10)
δ_{HCH}			1479	10	32	δ_{HCH} (58)
δ_{HCH}			1475	29	37	δ_{HCH} (15)
δ_{HCH}			1474	2	38	δ_{HCH} (26) + Γ_{HCCH} (14) + δ_{NCH} (12) + Γ_{CCCH} (5)
δ_{HCH}			1471	1	40	δ_{HCH} (18) + Γ_{HCCH} (6)
δ_{HCH}			1470	7	41	δ_{HCH} (17) + Γ_{HCCH} (17) + Γ_{NCCH}

						(5)
Γ_{HCCH}			1466	10	43	Γ_{HCCH} (20) + δ_{HCH} (19)
δ_{HCH}		1463	1464	6	43	δ_{HCH} (58)
δ_{HCH}			1461	12	40	δ_{HCH} (49)
δ_{HCH}			1459	18	35	δ_{HCH} (11)
δ_{CNH}			1459	11	35	δ_{CNH} (19) + ν_{CN} (13) + ν_{CO} (12)
ν_{CC}		1447	1446	17	19	ν_{CC} (37) + δ_{CCH} (12) + δ_{COH} (9)
ν_{CN}			1445	39	20	ν_{CN} (24) + δ_{CNH} (21) + ν_{CO} (7)
δ_{CNH}			1443	116	20	δ_{CNH} (20) + ν_{CN} (18) + ν_{CO} (7)
δ_{COH}			1431	280	7	δ_{COH} (61) + ν_{CO} (26)
ν_{CN}			1406	157	16	ν_{CN} (32) + ν_{CC} (14) + δ_{CNH} (10) + δ_{NCO} (7)
δ_{CNH}		1400	1401	10	11	δ_{CNH} (26) + ν_{CC} (10) + δ_{NCH} (8)
δ_{CCH}			1396	32	7	δ_{CCH} (18) + δ_{NCH} (11) + δ_{CNH} (9) + ν_{CN} (9) + ν_{CC} (8)
ν_{CN}	1391		1386	90	8	ν_{CN} (26) + δ_{CNH} (25) + ν_{CC} (12)
ν_{CC}			1384	4	9	ν_{CC} (25) + δ_{CCH} (12)
δ_{CCH}			1380	25	10	δ_{CCH} (17) + δ_{NCH} (9) + ν_{CC} (8) + ν_{CN} (6)
δ_{CCH}			1379	4	10	δ_{CCH} (40) + δ_{HCH} (17) + ν_{CC} (8)
ν_{CC}			1373	2	8	ν_{CC} (32) + δ_{CCH} (6) + δ_{NCH} (5)
δ_{CCH}			1360	2	11	δ_{CCH} (32) + ν_{CC} (22) + δ_{HCH} (7)
ν_{CC}			1355	30	17	ν_{CC} (18) + δ_{CCH} (15) + ν_{CN} (7)
ν_{CC}			1355	26	17	ν_{CC} (67)
ν_{NC}			1347	62	23	ν_{NC} (9)
δ_{CNH}			1346	22	25	δ_{CNH} (5)
δ_{CCH}			1342	63	31	δ_{CCH} (12) + ν_{CC} (8) + Γ_{HCCH} (6) + δ_{NCH} (5)
ν_{NC}			1340	52	33	ν_{NC} (19) + ν_{CC} (9)
δ_{CCH}			1332	61	61	δ_{CCH} (33) + ν_{CC} (26)
δ_{CCH}			1331	1	60	δ_{CCH} (11) + Γ_{NCCH} (7) + Γ_{CCCH} (6)
δ_{CNH}			1331	44	60	δ_{CNH} (36) + ν_{CN} (10) + δ_{NCH} (6)
δ_{CNH}		1329	1328	189	43	δ_{CNH} (18) + δ_{COH} (6) + ν_{CN} (6)
δ_{CNH}			1320	35	19	δ_{CNH} (32) + δ_{NCH} (14) + δ_{CCH} (6)
δ_{COH}			1320	71	19	δ_{COH} (36) + ν_{CO} (18) + ν_{CC} (8)
δ_{CCH}	1314		1310	28	13	δ_{CCH} (7)
δ_{CCH}			1309	23	13	δ_{CCH} (51) + δ_{COH} (10)
δ_{CNH}			1303	12	13	δ_{CNH} (4)
δ_{CNH}			1296	48	20	δ_{CNH} (14) + ν_{CO} (12) + ν_{CC} (5)
δ_{COH}			1292	52	29	δ_{COH} (33) + ν_{CO} (17) + ν_{CC} (7)
δ_{CCH}			1291	9	31	δ_{CCH} (27) + δ_{CNH} (6)
δ_{CCH}			1290	34	32	δ_{CCH} (30)
δ_{CCH}			1285	2	26	δ_{CCH} (31)
δ_{CCH}			1276	2	15	δ_{CCH} (6)
δ_{CCH}			1268	10	19	δ_{CCH} (17) + δ_{COH} (7) + ν_{CC} (6)
ν_{NC}			1267	52	19	ν_{NC} (15)
ν_{CO}	1245	1253	1249	111	18	ν_{CO} (54) + ν_{CC} (20)
δ_{CCH}			1247	1	17	δ_{CCH} (13)
δ_{CCH}			1238	33	10	δ_{CCH} (23) + ν_{CN} (13) + Γ_{HNCH} (5)
ν_{NC}			1232	49	11	ν_{NC} (8) + δ_{CNH} (6)
ν_{OH}			1228	21	13	ν_{OH} (5)
δ_{CNH}			1216	17	26	δ_{CNH} (12) + ν_{OH} (8) + ν_{CN} (7)

ν_{CC}			1214	7	28	ν_{CC} (29) + ν_{NC} (15)
ν_{CC}		1211	1209	1	25	ν_{CC}(26) + ν_{CN}(12)+ δ_{CCH}(13)
ν_{CN}			1208	5	24	ν_{CN}(25) + ν_{CC}(12) + δ_{CCH}(7)+ δ_{CNH}(7)
δ_{CCH}			1203	16	18	ν_{CN}(9) + ν_{OH}(5) + δ_{CCH}(12)
ν_{CN}			1182	9	7	ν_{CN}(33)
ν_{CN}		1178	1175	33	10	ν_{CN}(23) + δ_{CNH}(11)
ν_{CC}	1170		1172	8	10	ν_{CC}(31) + δ_{CCH}(26) + ν_{CN}(9)
δ_{CCH}			1160	3	20	δ_{CCH}(58) + δ_{COH}(10)
δ_{CCH}			1159	11	21	ν_{CN}(10) + ν_{CO}(7) + δ_{CCH}(15)
δ_{COH}			1157	232	21	ν_{CC}(11) + ν_{CO}(8) + δ_{CCH}(13) + δ_{COH}(56)
ν_{CN}			1153	8	15	ν_{CN}(24) + ν_{CC}(14) + δ_{CCH}(13)
ν_{CN}			1147	64	10	ν_{CN}(41) + δ_{CNH}(18)
δ_{CNH}			1136	13	10	ν_{CN}(17) + ν_{CC}(20) + δ_{CNH}(21)
ν_{CO}			1133	21	9	ν_{CO}(42) + ν_{CC}(6) + δ_{COH}(10)
δ_{CNH}			1119	28	12	ν_{CN}(30) + δ_{CNH}(34)
ν_{CC}			1117	2	13	ν_{CC}(53) + δ_{CCH}(13)
ν_{CN}			1109	13	16	ν_{CN}(30) + ν_{CC}(6) + δ_{CNH}(14)
ν_{CN}	1110		1109	31	16	ν_{CN}(20) + ν_{CO}(11) + δ_{CCH}(18)
δ_{CNH}			1094	35	14	ν_{CC}(11) + ν_{CN}(5) + δ_{CNH}(16)
ν_{CC}			1087	6	25	ν_{CC}(41) + ν_{CN}(7) + δ_{CCC}(7)
ν_{CN}			1086	14	25	ν_{CN}(24) + ν_{CC}(7) + δ_{CCH}(6)
ν_{CN}			1081	12	21	ν_{CN}(27) + ν_{CC}(12)
ν_{CN}			1080	7	21	ν_{CN}(32)+ ν_{CC}(13)
δ_{CNH}			1075	2	16	ν_{CN}(33) + ν_{CC}(8) + δ_{CNH}(41)
ν_{CC}			1066	10	9	ν_{CN}(14) + ν_{CC}(39)
ν_{CC}			1052	1	12	ν_{CC}(68)
ν_{CC}			1043	5	12	ν_{CC}(48) + δ_{CNH}(8)
ν_{CC}			1038	9	14	ν_{CC}(23) + ν_{CN}(13) + δ_{CNH}(18)
ν_{CC}		1027	1018	2	30	ν_{CC}(62)
ν_{CC}			1016	38	26	ν_{CC}(32)
δ_{CCC}			1007	1	8	ν_{CC}(20)+ δ_{CCH}(9)+ δ_{CCC}(24)
ν_{CN}			987	1	15	ν_{CC}(28)+ ν_{CN}(35)
Γ_{COOH}			982	63	18	ν_{CC}(8) + Γ_{COOH}(24) + Γ_{CCOH}(21)
ν_{CC}			976	38	23	ν_{CC}(22) + Γ_{COOH}(12) + Γ_{CCOH}(8)
ν_{CC}			972	7	25	ν_{CC}(32) + Γ_{COOH}(9) + ν_{CO}(6) + δ_{CCC}(5)
ν_{CN}		965	963	36	13	ν_{CN}(19) + δ_{CNH}(7)
ν_{CC}			954	1	11	ν_{CC}(32) + δ_{CCH}(22)
Γ_{CCHH}			951	1	10	ν_{CC}(7)+ δ_{CCH}(7)+ Γ_{CCCH}(13)+ Γ_{CCHH}(26) + Γ_{CCOH}(6)
ν_{CC}			939	98	11	ν_{CC}(29) + δ_{CNH}(25)
Γ_{CCHH}			938	8	12	ν_{CC}(8) + Γ_{CCCH}(5) + Γ_{CCHH}(11)
ν_{CC}			937	14	12	ν_{CC}(13) + ν_{CO}(6)
ν_{CC}			930	6	16	ν_{CC}(46) + δ_{CCH}(25)
ν_{CC}			927	29	13	ν_{CC}(26) + δ_{CNH}(5)
ν_{CC}			917	7	13	ν_{CC}(24) + ν_{CO}(5) + Γ_{CCHH}(8)
ν_{CN}			913	46	14	ν_{CN}(23) + δ_{CNH}(15)
δ_{CCH}			912	6	14	ν_{CC}(10) + δ_{CCH}(54)
ν_{CC}			909	24	13	ν_{CC}(39) + ν_{CO}(8)
ν_{CC}			901	2	14	ν_{CC}(36)
ν_{CC}	880		893	39	16	ν_{CC}(19) + ν_{CN}(18) + δ_{CNH}(17)+ Γ_{CNHH}(7)

ν_{CC}			858	5	19	$\nu_{CC}(53)$
ν_{CC}		856	854	18	28	$\nu_{CC}(18)$
ν_{CC}			852	22	29	$\nu_{CC}(12) + \delta_{CNH}(10)$
ν_{CC}			850	25	26	$\nu_{CC}(34) + \nu_{CO}(8)$
ν_{CC}			843	41	17	$\nu_{CC}(22)$
ν_{CC}			835	11	29	$\nu_{CC}(22) + \delta_{CNH}(5)$
Γ_{CCCH}		832	834	6	28	$\Gamma_{CCCH}(43) + \Gamma_{CCOH}(18)$
Γ_{COOH}			823	85	20	$\nu_{OH}(9) + \Gamma_{COOH}(35) + \Gamma_{CCOH}(16)$
δ_{CNH}			817	110	18	$\nu_{CN}(10) + \delta_{CNH}(11)$
Γ_{CCCH}	807		809	15	15	$\Gamma_{CCCH}(48) + \Gamma_{CCOH}(27)$
ν_{CC}			800	2	10	$\nu_{CC}(7) + \delta_{CCC}(6)$
δ_{CNO}			785	3	14	$\delta_{CNO}(6)$
ν_{CO}			780	84	16	$\nu_{CO}(12) + \nu_{CC}(6) + \Gamma_{CCOH}(7)$
Γ_{CNOH}			773	11	14	$\Gamma_{CNOH}(10) + \Gamma_{CCNH}(5)$
Γ_{CCCN}			771	8	15	$\Gamma_{CCCN}(12)$
Γ_{CNNH}			765	209	20	$\Gamma_{CNNH}(67) + \delta_{CNH}(8)$
Γ_{CNOH}			760	27	19	$\Gamma_{CNOH}(4)$
Γ_{CCHH}			752	16	8	$\Gamma_{CCHH}(18)$
Γ_{CNOH}			742	44	7	$\Gamma_{CNOH}(14)$
δ_{CCC}			732	6	9	$\nu_{CO}(5) + \delta_{COO}(6) + \delta_{CCC}(8) + \Gamma_{CCOH}(7)$
ν_{CC}	719		721	14	16	$\nu_{CC}(18)$
Γ_{CNNH}			713	9	15	$\delta_{CNH}(6) + \Gamma_{CNNH}(40)$
Γ_{CCNH}			706	43	15	$\Gamma_{CCNH}(34) + \Gamma_{CNOH}(7) + \Gamma_{CNHH}(6)$
δ_{COO}			703	16	16	$\delta_{COO}(7) + \nu_{CC}(6) + \nu_{CO}(6)$
Γ_{CCNH}			699	19	14	$\Gamma_{CCNH}(25) + \Gamma_{CNOH}(10)$
Γ_{CCNH}			692	47	10	$\Gamma_{CCNH}(25) + \Gamma_{CNOH}(7)$
Γ_{CCNH}			674	32	17	$\Gamma_{CCNH}(32)$
Γ_{CCNH}			673	73	17	$\Gamma_{CCNH}(21) + \delta_{COO}(8)$
δ_{CCC}		648	646	0	15	$\delta_{CCC}(56)$
Γ_{CCNH}			640	2	12	$\delta_{COO}(9) + \delta_{CCO}(5) + \Gamma_{CCNH}(13)$
δ_{CNN}			632	38	19	$\nu_{CN}(15) + \delta_{CNN}(25)$
Γ_{CCNH}			626	13	14	$\Gamma_{CCNH}(41)$
Γ_{CCNH}			623	40	13	$\Gamma_{CCNH}(33) + \delta_{CCO}(7)$
δ_{CNH}			614	145	13	$\delta_{CNH}(30) + \delta_{NHH}(5) + \Gamma_{CNNH}(11) + \Gamma_{CCNH}(6)$
Γ_{CCNH}			592	56	9	$\Gamma_{CCNH}(53) + \Gamma_{CNOH}(12) + \Gamma_{CNHH}(11)$
δ_{CCN}			585	82	12	$\delta_{CCN}(23) + \Gamma_{CCNH}(22)$
ν_{CC}			564	54	9	$\nu_{CC}(13) + \Gamma_{CCNH}(13)$
Γ_{CNHH}			556	103	10	$\delta_{CNH}(6) + \Gamma_{CCNH}(10) + \Gamma_{CNHH}(17) + \Gamma_{CNNH}(7)$
δ_{CCC}			553	37	9	$\delta_{CCC}(7)$
δ_{CNO}			536	31	7	$\nu_{CC}(7) + \delta_{CNO}(9) + \delta_{CCN}(9) + \Gamma_{CCNH}(5)$
δ_{CCN}			522	5	5	$\delta_{CCC}(8) + \delta_{CCN}(13)$
δ_{CCN}			510	4	10	$\delta_{CCN}(7)$
δ_{CCC}		499	510	8	10	$\delta_{CCC}(4)$
δ_{CCC}			482	18	15	$\delta_{CCC}(21) + \nu_{CO}(6)$
δ_{CNN}			472	27	11	$\delta_{CCC}(5) + \delta_{CNN}(10)$
δ_{CNN}			467	49	13	$\delta_{CNN}(20) + \Gamma_{CNHH}(5) + \Gamma_{CCNH}(7)$
δ_{CCO}			466	7	13	$\delta_{CCO}(23)$
δ_{CCO}			448	12	10	$\delta_{CCO}(25) + \nu_{CN}(21)$
δ_{CCC}			429	13	11	$\delta_{CCC}(8)$

δ_{CCN}			425	25	11	$\nu_{OH}(5)+ \delta_{CCC}(5) + \delta_{CCN}(6)$
δ_{CCO}			424	3	10	$\delta_{CCC}(12) + \delta_{CCO}(38)$
Γ_{CCCC}			419	2	7	$\Gamma_{CCCC}(19) + \delta_{CCO}(18)$
δ_{CCC}			408	29	7	$\delta_{CCC}(11) + \delta_{CCO}(11)$
Γ_{CNHH}			394	16	9	$\Gamma_{CNHH}(14) + \Gamma_{CCNH}(6)$
Γ_{CNHH}			390	40	8	$\Gamma_{CNHH}(31) + \Gamma_{CCNH}(18)$
ν_{OH}			364	1	17	$\nu_{OH}(11)$
ν_{OH}			358	21	27	$\nu_{OH}(10) + \Gamma_{CNHH}(6)$
ν_{OH}			356	16	31	$\nu_{OH}(6) + \Gamma_{CNHH}(6)$
Γ_{CCOH}			352	116	31	$\Gamma_{CCOH}(87)$
Γ_{CCNH}			345	12	17	$\Gamma_{CCNH}(14) + \delta_{CCO}(7)$
Γ_{CNNH}			337	6	19	$\Gamma_{CNNH}(52)$
Γ_{CNNH}			334	44	20	$\Gamma_{CNNH}(36)$
δ_{CCC}			331	8	18	$\delta_{CCC}(14)$
ν_{OH}			325	9	14	$\nu_{OH}(5)$
Γ_{CCCN}			310	7	16	$\Gamma_{CCCN}(5)$
Γ_{CCCN}			305	5	24	$\Gamma_{CCCN}(9) + \Gamma_{CCNO}(6)$
Γ_{CCCN}			304	7	24	$\Gamma_{CCCN}(6)$
δ_{CCN}			291	2	16	$\delta_{CCN}(7)+ \Gamma_{CCCN}(7) + \Gamma_{CCHH}(6)$
δ_{CCC}			282	2	25	$\delta_{CCC}(4)$
Γ_{CCCH}			280	0	24	$\Gamma_{CCCH}(34)$
δ_{CCC}			266	2	26	$\delta_{CCC}(14)$
Γ_{CCCH}			261	7	27	$\Gamma_{CCCH}(24)$
Γ_{CCCH}			251	1	20	$\Gamma_{CCCH}(56)$
Γ_{CCNH}			242	47	29	$\Gamma_{CCNH}(78)+ \Gamma_{CNHH}(12)$
Γ_{CCNH}			238	25	26	$\Gamma_{CCNH}(44)$
δ_{COH}			232	4	21	$\delta_{CCC}(6) + \delta_{COH}(7) + \nu_{OH}(7)$
Γ_{CCCN}			214	5	25	$\Gamma_{CCCN}(7)$
δ_{CCN}			204	5	19	$\delta_{CCN}(18) + \Gamma_{CCCC}(6)$
δ_{CCC}			196	1	26	$\delta_{CCC}(9)$
Γ_{CCCN}			188	2	35	$\delta_{CCC}(7) + \Gamma_{CCCN}(15)$
ν_{OH}			182	12	37	$\nu_{OH}(31)$
ν_{OH}			177	5	41	$\nu_{OH}(8)$
Γ_{CCNN}			173	6	42	$\nu_{OH}(5) + \Gamma_{CCNN}(11)$
Γ_{CCCN}			167	3	34	$\Gamma_{CCCN}(6) + \Gamma_{CCNH}(6)$
Γ_{CCCN}			161	3	36	$\Gamma_{CCCN}(9)$
δ_{CCC}			159	5	35	$\delta_{CCC}(12)+ \Gamma_{CCNN}(8) + \Gamma_{CCCN}(5)$
δ_{CCC}			155	6	32	$\delta_{CCC}(5)$
Γ_{CCCN}			142	4	44	$\Gamma_{CCCN}(5)$
Γ_{CCCC}			138	3	44	$\Gamma_{CCCC}(7) + \Gamma_{CCCN}(6)$
Γ_{CCCN}			125	2	56	$\Gamma_{CCCN}(21)+ \Gamma_{CCNH}(5)$
Γ_{CCCN}			119	4	79	$\Gamma_{CCCN}(7)$
Γ_{CCCN}			114	2	86	$\Gamma_{CCCN}(20) + \Gamma_{CCNH}(6)$
Γ_{CCNH}			111	6	92	$\Gamma_{CCNH}(7)$
Γ_{CCCN}			105	6	104	$\Gamma_{CCCN}(11)$
Γ_{CCCC}			97	1	124	$\Gamma_{CCCC}(4)$
Γ_{CCCN}			89	1	201	$\Gamma_{CCCN}(5)$
Γ_{CCCN}			84	2	244	$\Gamma_{CCCN}(18)$
Γ_{CCCN}			79	2	297	$\Gamma_{CCCN}(25)$
Γ_{CCCN}			76	3	322	$\Gamma_{CCCN}(14)$
Γ_{CCCN}			74	0	314	$\Gamma_{CCCN}(27) + \Gamma_{CCNO}(8) + \Gamma_{CCNN}(6)$
Γ_{CCCN}			67	2	371	$\Gamma_{CCCN}(9)$
Γ_{CCCH}			62	3	511	$\Gamma_{CCCH}(3)$

Γ_{CCCN}			59	1	578	$\Gamma_{CCCN}(14) + \Gamma_{CCNH}(11)$
Γ_{CCCN}			55	1	708	$\Gamma_{CCCN}(5)$
Γ_{CCNO}			50	0	1080	$\Gamma_{CCNO}(20) + \Gamma_{CCCO}(9) + \Gamma_{COOH}(7) + \Gamma_{CCOH}(13)$
Γ_{CCCN}			47	1	1470	$\Gamma_{CCCN}(39) + \Gamma_{CCNN}(7)$
Γ_{CCCN}			43	2	2100	$\Gamma_{CCCN}(6)$
Γ_{CCCN}			43	0	2100	$\Gamma_{CCCN}(26)$
Γ_{CCNN}			39	0	1810	$\Gamma_{CCNN}(4)$
Γ_{CCCC}			33	0	1360	$\Gamma_{CCCC}(9)$
Γ_{CCCN}			29	0	1570	$\Gamma_{CCCN}(23)$
Γ_{CCCN}			24	0	1670	$\Gamma_{CCCN}(29) + \Gamma_{CCNH}(6)$
Γ_{CCCN}			16	0	2830	$\Gamma_{CCCN}(6)$
Γ_{CCNN}			11	1	5110	$\Gamma_{CCNN}(10) + \Gamma_{CCCN}(10) + \Gamma_{CCNO}(9) + \Gamma_{CCCO}(9) + \Gamma_{CCNH}(5)$
Γ_{CCNH}			10	0	5270	$\Gamma_{CCNN}(8) + \Gamma_{CCCN}(7) + \Gamma_{CCNO}(7) + \Gamma_{CCCO}(6) + \Gamma_{CCNH}(11)$
Γ_{CCCN}			8	1	4700	$\Gamma_{CCCN}(18)$

Molecular electrostatic potential

The magnitude of the electrostatic potential is depicted using a color gradient. The electrostatic potential follows an increasing order from red to blue, progressing through orange, yellow, and green. The red regions correspond to areas of maximum electronegativity (most negative potential), while the blue regions indicate areas of maximum electropositivity (most positive potential). This representation highlights the regions of positive potential within the molecule, corresponding to electrophilic sites, as well as regions of negative potential, indicative of nucleophilic attack sites and possible hydrogen bond interaction sites [35]. The regions with negative potential values were concentrated on oxygen and nitrogen, whereas regions with positive potentials were concentrated on hydrogen atoms of NH_2, NH, CH, CH_2 and CH_3 groups.

The range of colors in the MEP map of thymopentin is -0.07017 a.u. (deepest red) to +0.07017 a.u. (deepest blue). Dark blue and dark red represent the corresponding potential differences, which are -1.909 V (dark red) and 1.909 V (dark blue), respectively.

HOMO and LUMO energies

A molecule's energy gap between its HOMO-LUMO can reveal information about its biochemical activity and the flow characteristics of its electric charge and is related to its reactivity and the smaller the gap energy, the more reactive the molecule is [36]. A large energy gap indicates lower molecular polarization, characterizing the molecule as "hard," which correlates with higher chemical stability and lower reactivity [37]. For the compound under investigation, the HOMO-LUMO energy gap (ΔE) in the gas phase is calculated to be 5.1 eV, reflecting its chemical stability and reactivity profile.

Utilizing the Time-Dependent Density Functional Theory (TD-DFT) and the B3LYP/6-31G(d,p) basis set, the electronic transitions of thymopentin in gas phases were computed. It was discovered that thymopentin had an energy gap of 4.762 eV between its ground singlet state and its first excited singlet state. An analysis was conducted using the GaussSum (Version 3.0) tool to determine the contribution of atomic orbitals to HOMO and LUMO (Frontier Orbitals) [38]. The calculated absorption maximum value for the thymopentin molecule is 260.4 nm (f = 0.0017). This value is corresponding to the excited state S0→S1, which includes the transition from HOMO to LUMO. The absorption of the excited state S0 →S2 is 246.1 nm (f = 0.0025), and involving two configurations (HOMO- > L+1, HOMO- > L+2). The absorption of the

excited state S0 →S3 is 245.7 nm (f = 0.0126), and involving three configurations (H-1- > LUMO, H-1- > L+1, H-1- > L+2). The absorption of the excited state S0 →S4 is 245.0 nm (f = 0.0107), and involving three configurations (H-1-> LUMO, H-1- > L+1, H-1- > L+2). The absorption of the excited state S0 →S5 is 240 nm (f = 0), and involving one configuration (H-2- >LUMO). The absorption of the excited state S0 →S6 is 237.3 nm (f = 0.0014), and involving three configurations (H-3- > LUMO, HOMO- > L+1, HOMO- > L+2).

Molecular docking

Using protein databank (http://www.rcsb.org/pdb) molecular docking calculations were performed for the crystal structure of the following crystal structures: DNA (PDB ID: 1BNA), EGFR tyrosine kinase (PDB ID: 4HJO), apo form of COVID-19 Mpro (PDB ID: 6M03).
The Autodock Vina software [39] was used to carry out molecular docking simulations, and the CAVER program [40] was utilized to search receptor active sites. Prior to the docking analysis, polar hydrogens were included and water molecules were extracted from the target protein.
The optimized thymopentin structure was modified for docking, and the target's Kollman charges were ascertained.

The Geistenger technique was utilized to compute the partial charges of the thymopentin molecule. The target's active area was determined to have dimensions of 40x40x40 Å. By altering its rotatable torsions, thymopentin was handled as a flexible ligand during docking, whereas the target protein was regarded as a stiff receptor.

The program created by Wang *et al.* [41] utilized the MM/PB(GB)SA approach for computing the binding free energies and the Groningen Machine for Chemical Simulations (GROMACS) software package [42-46] performed molecular dynamics (MD) simulations of the ligand-receptor complexes of thymopentin with SARS-CoV-2 enzyme (6M03) and EGFR tyrosine kinase (PDB ID: 4HJO) and applying GROMOS96 43a1 force field [47,48].

For molecular dynamics (MD) simulation, the thymopentin-protein complex with a minimal binding energy was chosen. The ligand-protein combination was solved in a triclinic periodic box by applying the simple point charge (SPC) water system. Next, 0.15M NaCl salt was put into the solution to neutralize it, and energy minimization was carried out using the steepest descent technique for 50,000 steps.

The MD simulations were configured using the GROMACS equilibration settings of constant temperature (T) of 300 K, constant volume (V), constant number of atoms (NVT), and constant pressure (P) of 1.0 bar.

The stability of the ligand-enzyme complexes was tested using a Leap-frog MD integrator, an approximate number of frames per simulation set to 1000, and MD simulation run for 50 ns.
The root-mean-square deviation (RMSD), root-mean-square fluctuations (RMSF), radius of gyration (Rg), protein-ligand hydrogen bonding, and solvent-accessible surface area (SASA) were measured and assessed to examine the simulated trajectories.

Figures 4 and 5 display the thymopentin docking result in the active site of 6M03 and 4HJO respectively, and the interacting residues.

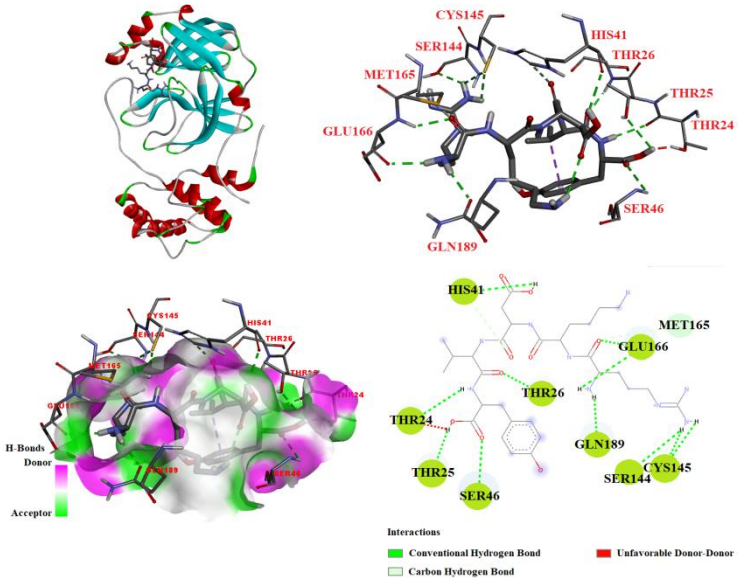

Figure 4. The 3D docked views of the most stable conformer of thymopentin in SARS-CoV-2 main protease (6M03). The ligand interaction diagrams of receptor-ligand complexes are shown.

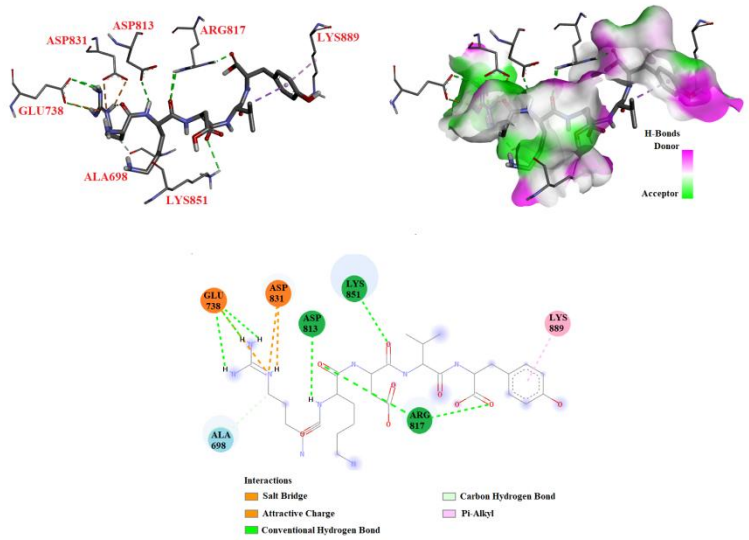

Figure 5. The 3D docked views of the most stable conformer of thymopentin in EGFR tyrosine kinase (PDB ID: 4HJO). The ligand interaction diagrams of receptor-ligand complexes are shown.

Table 3. Binding affinity and interacting residues between target protein and thymopentin

Target protein	Binding affinity (kcal/mol)	Number of bonded residues	Bonded residues
DNA (1BNA)	-6.8	6	DG2(2.29); DG4(3.59;2.42;2.7); DA5(3.35;3.28;2.8;3.58;2.09); DT20(2.6;2.9); DC21(2.39;2.58); DG22(2.23)
SARS-CoV-2 M^{pro} (6M03)	-6.8	10	THR24(1.33;2.59); THR25(2.87); THR26(2.02); HIS41(2.54;3.48); SER46(2.86); SER144(2.46); CYS145(2.66;2.88); MET165(3.25); GLU166(2.18;2.37); GLN189(2.29)
EGFR (4HJO)	-6.6	7	ALA698(3.4); GLU738(2.5;2.86;3.05;4.08); ASP813(2.53); ARG817(2.65;3.02); ASP831(2.66;3.41); LYS851(3.01); LYS889(3.73)

Table 3 presents an overview of the molecular docking simulation results and lists the interacted residues and binding affinities between thymopentin and target proteins. Figures 4 and 5 illustrate the molecular docking of thymopentin into target proteins.

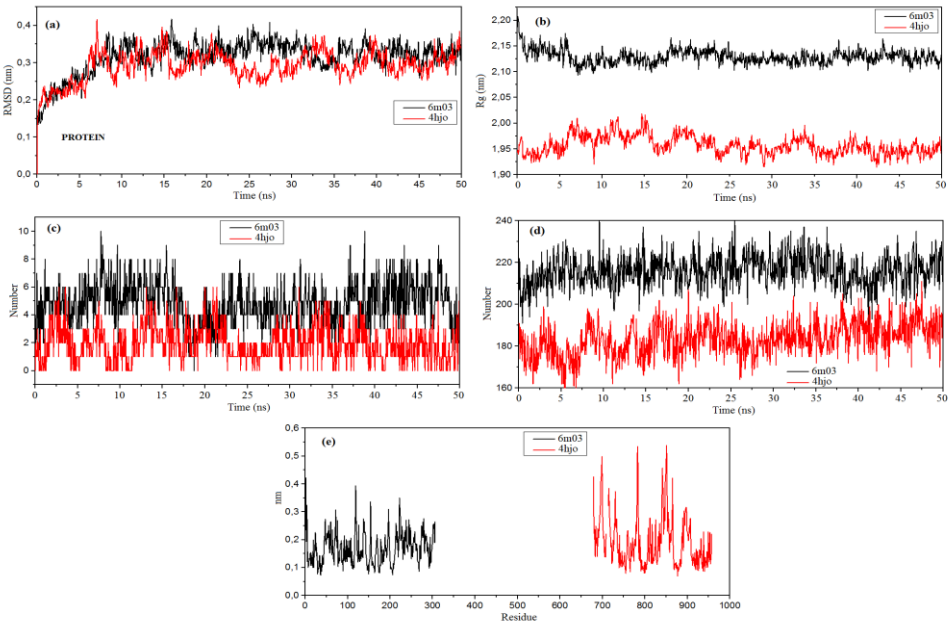

Figure 6. Analysis of structural stability and simulation results of thymopentin-6M03 and thymopentin-4HJO complexes. Protein root mean square deviation (RMSD) plot (a), Radius of gyration (Rg) plot (b), ligand H-bond plot (c), H-bond plot (d) and root mean square fluctuation (RMSF) plot (e).

When comparing various atomic conformations of a given molecular system, the root mean square deviation (RMSD) of a protein or ligand is utilized. The value indicates the extent of conformational change in the ligand or protein. The complexes are stable if there are only minor conformational changes in the protein, as indicated by a small variation in the RMSD value. Nonetheless, the RMSD value's deviations are more significant than its mean value. A small deviation suggests that the structure of the ligand or protein has undergone minor conformational changes. It is widely acknowledged that a ligand-protein complex is stable if the deviation in the RMSD graph is less than 4 Å. In this work, the displacement of the ligand or protein relative to the starting position was determined by performing independent RMSD analyses for the ligand and the target protein. The degree of structural deviation of the complexes' Cα atoms during 50 ns simulations is displayed in the protein's RMSD plot, as shown in figure 6. The protein backbone (PDB ID: 6M03) in complex with thymopentin has an average RMSD of 3.2 Å and a range of 1.83 to 4.17 Å. The protein's RMSD for the thymopentin-4HJO complex is 1.8 to 4.17 Å, with an average of 2.94 Å (see figure 6). The degree of structural deviation of the ligand atoms in the complexes (6M03 and 4HJO) during 50 ns simulations is displayed in the RMSD plot of the ligand (figure 6). It was noted that the trajectory of the thymopentin complexes fluctuated at first, but after 10 ns it stabilized and stayed that way for 50 ns.

In silico structure-based pharmacological prediction

The thymopentin was tested in vitro against a set of bacteria and different cell lines of chondrosarcoma to evaluate their antibacterial and anticancer properties.

Antibacterial activity

Using AntiBac-Pred web service, a web application for predicting the antibacterial activity of compounds, the antibacterial activities of the thymopentin against different bacteria strains were searched [49]. Thymopentin has been shown to be effective against a wide range of bacteria.

Anticancer sensitivity prediction

The anti-cancer activity of thymopentin was searched against different cell lines of chondrosarcoma by using PaccMann database [50] and canonical SMILES of the molecule. The IC_{50} (half maximal inhibitory concentration) is used as an indicator of the cytotoxicity of anticancer drugs in vitro. It was found that thymopentin was predicted to exhibit anticancer activity against various cell lines.

CONCLUSION

In the study, the structural, vibrational, electronic, and biological properties of thymopentin, that has a wide variety of biological activities, were evaluated with the aid of quantum chemical computations. A complete vibrational analysis of thymopentin was performed at DFT/B3LYP/6-31G(d,p) level of theory, and experimental and theoretical IR and Raman spectra of the title molecule were reported. Also, HOMO and LUMO energies and the molecular electrostatic potential (MEP) of thymopentin have also been calculated, which are very useful properties in prediction of molecular reactive behavior. The docking simulations were performed for evaluation of the biological activity of the thymopentin molecule, using its most stable structure. The radius of gyration (Rg) and root mean square deviation (RMSD) values were employed during the dynamic simulation to assess structural deviations, determining whether the protein experienced any distortion or maintained its conformational stability over

the 50-ns simulation period. The structural deviation of the ligand atoms in the complexes (6M03 and 4HJO) during 50 ns simulations is shown that the Thymopentin complexes fluctuated at first, but after 10 ns it stabilized and stayed that way for 50 ns. The in vitro antimicrobial activity of the compound on the agar plate was determined on gram positive and gram-negative bacteria, and the results are presented. Antibacterial activity was observed on *L. monocytogenes* and *B. cereus*. It did not show any effect on *S. aureus* from gram-positive bacteria and against gram-negative bacteria. Thymopentin compound has been determined to have an antimicrobial effect against gram-positive bacteria. Antifungal activity was seen against *P.expansum*. This informations are crucial for guiding the design and development of more potent compounds in future research.

ACKNOWLEDGEMENTS

This work was supported by the Scientific Research Projects Coordination Unit of Istanbul University [ÖNAP-2423].

Disclosure statement

The authors declare that they have no competing interests.

Data availability

The data that support the findings of this study are available from the corresponding author upon reasonable request.

REFERENCES

1. Goldstein, G.; Audhya, T.K. Thymopoietin to thymopentin: Experimental studies. *Surv. Immunol. Res.* **1985**, 4, 1-10.
2. Zdrojewicz, Z.; Pachura, E.; Pachura, P. The thymus: A forgotten, but very important organ. *Adv. Clin. Exp. Med.* **2016**, 25, 369-375.
3. Tosti, A.; Manuzzi, P.; Gasponi, A. Thymopentin in the treatment of severe alopecia areata. *Dermatology* **1988**, 177, 170-174.
4. Gallo, F.; Morale, M.C.; Sambataro, D.; Farinella, Z.; Scapagnini, U.; Marchetti, B. The immune system response during development and progression of carcinogen-induced rat mammary tumors: prevention of tumor growth and restoration of immune system responsiveness by thymopentin. *Breast Cancer Res. Treat.* **1993**, 27, 221-237.
5. Hambley, T.W. Is anticancer drug development heading in the right direction? *Cancer Res.* **2009**, 69, 1259-1262.
6. Lao, X.; Li, B.; Liu, M.; Chen, J.; Gao, X.; Zheng, H. Increased antitumor activity of tumor-specific peptide modified thymopentin. *Biochimie*. **2014**, 107, 277-285.
7. Sundal, E.; Bertelletti, D. Management of viral infections with thymopentin. *Arzneimittel-forschung*. **1994**, 44, 866-871.
8. Bodey, B.; Bodey Jr, B.; Siegel, S.E.; Kaiser, H.E. Review of thymic hormones in cancer diagnosis and treatment. *Int. J. Immunopharmacol.* **2000**, 22, 261-273.
9. Gonser, S.; Weber, E.; Folkers, G. Peptides and polypeptides as modulators of the immune response: thymopentin-an example with unknown mode of action. *Pharm. Acta Helv.* **1999**, 73, 265-273.
10. Application of thymopentin in preparation of drug for treating patient with severe hepatitis b, patent CN103656614A

11. Solmajer, T. Design of a novel thymopoietin analogue based on conformational analyses. *Drug Des. Deliv.***1990**, 6, 213-221.
12. Tan, Y.; Wang, W.; Wu, C.; Pan, Z.; Yao, G.; Fang, L.; Su, W. Myristic acid-modified thymopentin for enhanced plasma stability and immune-modulating activity. *Int. Immunopharmacol.* **2017**, 47, 88-94.
13. Islam, M.A.; Haque, M.A.; Rahman, M.A.; Hossen, F.; Reza, M.; Barua, A.; Marzan, A.A.; Das, T.; Baral, S.K.; He, C.; Ahmed, F.; Bhattacharya, P.; Jakariya, M. A review on measures to rejuvenate immune system: natural mode of protection against coronavirus infection. *Front. immunol.* **2022**, 13, 837290.
14. Mander, L.; Liu, H.W. *Comprehensive Natural Products II: Chemistry and Biology* (Vol. 1). Elsevier, **2010**.
15. Buzia, O.D.; Dima, C.; Dima, S. Preparation and characterization of chitosan microspheres for vancomycin delivery. *Farmacia*. **2015**, 63, 897-902.
16. Senthilkumar, P.; Dawn, S.; Samanvitha, K.S.; Kumar, S.S.; Kumar, G.N.; Samrot, A.V. Optimization and characterization of poly [R] hydroxyalkanoate of *Pseudomonas aeruginosa* SU-1 to utilize in nanoparticle synthesis for curcumin delivery. *Biocatal. Agric. Biotechnol.* **2017**, 12, 292-298.
17. Erhonyota, C.; Edo, G.I.; Onoharigho, F.O. Comparison of poison plate and agar well diffusion method determining the antifungal activity of protein fractions. *Acta Ecol. Sin.* **2023**, 43, 684-689.
18. Shao, Y.; Molnar, L.F.; Jung, Y.; Kussmann, J.; Ochsenfeld, C.; Brown, S.T.; Gilbert A.T.; Slipchenko, L.V.; Levchenko, S.V.; O'Neill, D.P.; DiStasio, R.A.; Lochan, R.C.; Wang, T.; Beran, G.J.; Besley, N.A.; Herbert, J.M.; Lin, C.Y.; Voorhis T.V.; Chien, S.H.; Sodt, A.; Steele, R.P.; Rassolov, V.A.; Maslen, P.E.; Korambath, P.P.; Adamson, R.D.; Austin, B.; Baker, J.; Byrd, E.F.; Dachsel, H.; Doerksen, R.J.; Dreuw, A.; Dunietz, B.D.; Dutoi, A.D.; Furlani, T.R.; Gwaltney, S.R.; Heyden, A.; Hirata, S.; Hsu, C.P.; Kedziora, G.; Khalliulin, R.Z.; Klunzinger, P.; Lee, A.M.; Lee, M.S.; Liang, W.; Lotan, I.; Nair, N.; Peters, B.; Proynov, E.I.; Pieniazek, P.A.; Rhee, Y.M.; Ritchie, J.; Rosta, E.; Sherrill, C.D.; Simmonett, A.C.; Subotnik, J.E.; Woodcock, H.L.; Zhang, W.; Bell, A.T.; Chakraborty, A.K.; Chipman, D.M.; Keil, F.J.; Warshel, A.; Hehre, W.J.; Schaefer, H.F.; Kong, J.; Krylov, A.I.; Gill, P.M.; Head-Gordon, M. Advances in methods and algorithms in a modern quantum chemistry program package. *Phys. Chem. Chem. Phys.* **2006**, 8, 3172-3191.
19. Frisch, M.J.; Trucks, G.W.; Schlegel, H.B.; Scuseria, G.E.; Robb, M.A.; Cheeseman, J.R.; Scalmani, G.; Barone, V.; Petersson, G.A.; Nakatsuji, H.; Li, X.; Caricato, M.; Marenich, A.V.; Bloino, J.; Janesko, B.G.; Gomperts, R.; Mennucci, B.; Hratchian, H.P.; Ortiz, J.V.; Izmaylov, A.F.; Sonnenberg, J.L.; Williams-Young, D.; Ding, F.; Lipparini, F.; Egidi, F.; Goings, J.; Peng, B.; Petrone, A.; Henderson, T.; Ranasinghe, D.; Zakrzewski, V. G.; Gao, J.; Rega, N.; Zheng, G.; Liang, W.; Hada, M.; Ehara, M.; Toyota, K.; Fukuda, R.; Hasegawa, J.; Ishida, M.; Nakajima, T.; Honda, Y.; Kitao, O.; Nakai, H.; Vreven, T.; Throssell, K.; Montgomery, J.A.Jr.; Peralta, J.E.; Ogliaro, F.; Bearpark, M.J.; Heyd, J.J.; Brothers, E.N.; Kudin, K.N.; Staroverov, V.N.; Keith, T.A.; Kobayashi, R.; Normand, J.; Raghavachari, K.; Rendell, A.P.; Burant, J.C.; Iyengar, S.S.; Tomasi, J.; Cossi, M.; Millam, J.M.; Klene, M.; Adamo, C.; Cammi, R.; Ochterski, J.W.; Martin, R.L.; Morokuma, K.; Farkas, O.; Foresman, J.B.; Fox, D.J. Gaussian, Inc., Gaussian 16, Revision C.01, Wallingford CT, **2016**.
20. Rudbeck, M. *The beauty of the bitter devils: A theoretical study on phosphate molecules*. PhD Thesis, Stockholm University, Stockholm, Sweden, **2011**.
21. Sundius, T. Molvib-A flexible program for force field calculations. *J. Mol. Struct.* **1990**, 218, 321-326.
22. Pulay, P.; Fogarasi, G.; Pongor, G.; Boggs, J.E.; Vargha, A. Combination of theoretical ab initio and experimental information to obtain reliable harmonic force constants. Scaled

quantum mechanical (QM) force fields for glyoxal, acrolein, butadiene, formaldehyde, and ethylene. *J. Am. Chem. Soc.* **1983**, 105, 7037-7047.
23. Istvan K. Simirra, A Program for Simulation of IR and Raman Spectra, Chemical Research Center, Budapest, **2002** (It was obtained from Dr. Gabor Keresztury in Chemical Research Center in Budapest).
24. Eğlence-Bakır, S.; Celik, S.; Şahin, M.; Ozel, A.E.; Akyuz, S.; Ülküseven, B. Synthesis, molecular modelling, FT-IR, Raman and NMR characterization, molecular docking and ADMET study of new nickel(II) complex with an N4-tetradentate thiosemicarbazone. *J. Biomol. Struct. Dyn.* **2021**, 39, 4212-4224.
25. Onem, Z.O; Er, A.; Celik, S.; Ozel, A.E.; Akyuz, S. The significance of doxylamine, an antihistamine compound, in the context of its potential efficacy against Covid-19: Conformational analysis, molecular docking, and molecular dynamics studies. *SSRN* **2024**, 1-22. http://dx.doi.org/10.2139/ssrn.4778767.
26. Pitinidhipat, N.; Yasurin, P. Chrysanthemum indicum, Centella asiatica ve Andrographis paniculata'nın ozmotik stres altında Bacillus cereus ve Listeria monocytogenes'e karşı antibakteriyel aktivitesi. *AU Teknoloji Dergisi* **2012**, 15, 239-245.
27. Reboux, G.; Rocchi, S.; Vacheyrou, M.; Millon, L. Identifying indoor air Penicillium species: a challenge for allergic patients. *J. Med. Microbiol.* **2019**, 68, 812-821.
28. Courvoisier, E.; Williams, P.A.; Lim, G.K.; Hughes, C.E.; Harris, K.D. The crystal structure of l-arginine. *Chem.Comm*. **2012**, 48, 2761-2763.
29. Pratap, J.V.; Ravishankar, R.; Vijayan, M. X-ray studies on crystalline complexes involving amino acids and peptides. XXXV. Invariance and variability in amino acid aggregation in the complexes of maleic acid with L-histidine and L-lysine. *Acta Crystallogr. B Struct. Sci.* **2000**, 56, 690-696.
30. Derissen, J.L.; Endeman, H.J.; Peerdeman, A.F. The crystal and molecular structure of L-aspartic acid. *Acta Crystallogr. B* **1968**, 24, 1349-1354.
31. Torii, K.; Iitaka, Y. The crystal structure of L-valine. *Acta Crystallogr. B: Struct. Sci. Cryst.* **1970**, 26, 1317-1326.
32. Smalley, C.J.; Hoskyns, H.E.; Hughes, C.E.; Johnstone, D.N.; Willhammar, T.; Young, M. T.; Pickard, C.J.; Logsdail, A.J.; Midgley, P.A.; Harris, K.D. A structure determination protocol based on combined analysis of 3D-ED data, powder XRD data, solid-state NMR data and DFT-D calculations reveals the structure of a new polymorph of L-tyrosine. *Chem. Sci.* **2022**, 13, 5277-5288.
33. Mendham, A.P.; Dines, T.J.; Snowden, M.J.; Chowdhry, B.Z.; Withnall, R. Vibrational spectroscopy and DFT calculations of di-amino acid cyclic peptides. Part I: cyclo (Gly-Gly), cyclo (L-Ala-L-Ala) and cyclo (L-Ala-Gly) in the solid state and in aqueous solution. *J. Raman Spectrosc.* **2009**, 40, 1478-1497.
34. Mendham, A.P.; Dines, T.J.; Snowden, M.J.; Withnall, R.; Chowdhry, B.Z. IR/Raman spectroscopy and DFT calculations of cyclic di-amino acid peptides. Part III: Comparison of solid state and solution structures of cyclo (L-Ser-L-Ser). *J. Raman Spectrosc.* **2009**, 40, 1508-1520.
35. Kalaycı, T.; Kınaytürk, N.K.; Tunalı, B. Experimental and theoretical investigations (FTIR, UV-VIS spectroscopy, HOMO-LUMO, NLO and MEP analysis) of aminothiophenol isomers. *Bull. Chem. Soc. Ethiop.* **2021**, 35, 601-614.
36. Celik, S.; Ozel, A.E.; Durak, V., Akyuz, S. Vibrational spectroscopic characterization, quantum chemical and molecular docking studies of Valyl-Methionine dipeptide. *Spectrosc. Lett*. **2020**, 53, 648-663.
37. Pearson, R.G. Hard and Soft Acids and Bases (Van Nostrand Reinhold: New York, NY), **1973**, 2.
38. O'boyle, N.M.; Tenderholt, A.L.; Langner, K.M. Cclib: A library for package-independent computational chemistry algorithms. *J. Comput. Chem.* **2008**, 29, 839-845.

39. Trott, O.; Olson, A.J. AutoDock Vina: improving the speed and accuracy of docking with a new scoring function, efficient optimization, and multithreading. *J. Comput. Chem.* **2010**, 31, 455-461.
40. Jurcik, A.; Bednar, D.; Byska, J.; Marques, S.M.; Furmanova, K.; Daniel, L.; Kokkonen, P.; Brezovsky, J.; Strnad, O.; Stourac, J.; Pavelka, A.; Manak, M.; Damborsky, J.; Kozlikova, B. CAVER analyst 2.0: Analysis and visualization of channels and tunnels in protein structures and molecular dynamics trajectories. *Bioinformatics* **2018**, 34, 3586-3588.
41. Wang, Z.; Wang, X.; Li, Y.; Lei, T.; Wang, E.; Li, D.; Kang, Y.; Zhu, F.; Hou, T. FarPPI: A webserver for accurate prediction of protein-ligand binding structures for small-molecule PPI inhibitors by MM/PB (GB) SA methods. *Bioinformatics*, **2019**, 35, 1777-1779.
42. Abraham, M.J.; Murtola, T.; Schulz, R.; Pall, S.; Smith, J.C.; Hess, B.; Lindahl, E. GROMACS: High performance molecular simulations through multi-level parallelism from laptops to supercomputers. *SoftwareX* **2015**, 1, 19-25.
43. Bekker, H.; Berendsen, H.J.C.; Dijkstra, E.J.; Achterop, S.; Vondrumen, R.V.; Vanderspoel, D., Sijbers, A.; Keegstra, H.; Renardus, M.K.R. Gromacs-a parallel computer for molecular-dynamics simulations. In 4th international conference on computational physics (PC 92) (pp. 252-256), **1993**, World Scientific Publishing.
44. Bjelkmar, P.; Larsson, P.; Cuendet, M.A.; Hess, B.; Lindahl, E. Implementation of the CHARMM force field in GROMACS: Analysis of protein stability effects from correction maps, virtual interaction sites, and water models. *J. Chem. Theory Comput.* **2010**, 6, 459-466.
45. Lindorff-Larsen, K.; Piana, S.; Palmo, K.; Maragakis, P.; Klepeis, J.L.; Dror, R.O.; Shaw, D.E. Improved side-chain torsion potentials for the Amber ff99SB protein force field. *Proteins:Struct. Funct. Bioinf.* **2010**, 78, 1950-1958.
46. van Gunsteren, W.F.; Billeter, S.R.; Eising, A.A.; Hünenberger, P.H.; Krüger, P.K.H.C.; Mark, A. E.; Scott, W.R.P.; Tironi, I.G.; Tran, F.; Billeter, S.; Eising, A. A.; Hünenberger, P.; Kruger, P.; Mark, E.; Scott, R.; Tironi, I.G. Biomolecular simulation: the GROMOS96 manual and user guide. *Vdf Hochschulverlag AG an der ETH Zürich, Zürich* **1996**, 86, 1-1044.
47. Daura, X.; Mark, A.E.; Van Gunsteren, W.F. Parametrization of aliphatic CHn united atoms of GROMOS96 force field. *J. Comput. Chem.* **1998**, 19, 535-547.
48. Oostenbrink, C.; Villa, A.; Mark, A.E.; Van Gunsteren, W.F. A biomolecular force field based on the free enthalpy of hydration and solvation: the GROMOS force-field parameter sets 53A5 and 53A6. *J. Comput. Chem.* **2004**, 25, 1656-1676.
49. Pogodin, P.V.; Lagunin, A.A.; Rudik, A.V.; Druzhilovskiy, D.S.; Filimonov, D.A.; Poroikov, V.V. AntiBac-Pred: A web application for predicting antibacterial activity of chemical compounds. *J. Chem. Inf. Model.* **2019**, 59, 4513-4518.
50. Cadow, J.; Born, J.; Manica, M.; Oskooei, A.; Martínez, M.R. PaccMann: A web service for interpretable anticancer compound sensitivity prediction. *Nucleic Acids Res*, **2020**, 48, W502-W508.